

Harmonic linearized Navier-Stokes equation on describing the effect of surface roughness on hypersonic boundary-layer transition

Cite as: Phys. Fluids **31**, 034108 (2019); <https://doi.org/10.1063/1.5086912>

Submitted: 25 December 2018 . Accepted: 28 February 2019 . Published Online: 27 March 2019

Lei Zhao (赵磊) , Ming Dong (董明), and Yanguang Yang (杨彦广) 

COLLECTIONS

 This paper was selected as an Editor's Pick



View Online



Export Online



CrossMark

ARTICLES YOU MAY BE INTERESTED IN

[Is Tollmien-Schlichting wave necessary for transition of zero pressure gradient boundary layer flow?](#)

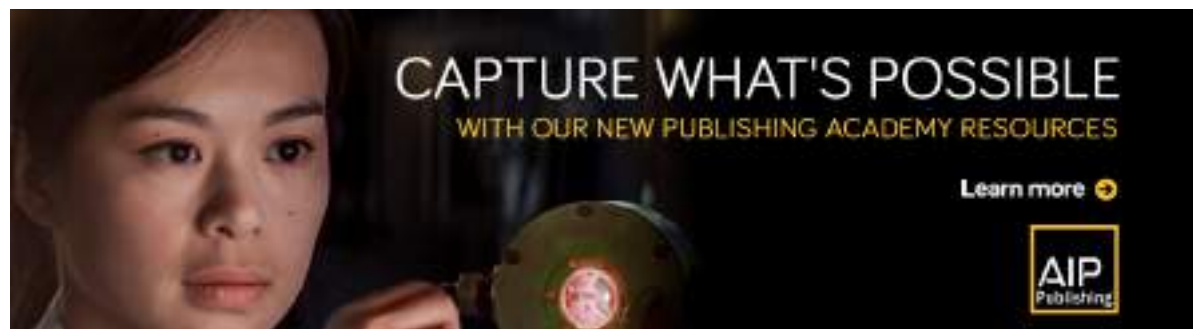
Physics of Fluids **31**, 031701 (2019); <https://doi.org/10.1063/1.5089294>

[On the inherent bias of swirling strength in defining vortical structure](#)

Physics of Fluids **31**, 035107 (2019); <https://doi.org/10.1063/1.5089883>

[Formation of water in oil in water particles by drop impact on an oil layer](#)



Physics of Fluids **31**, 037107 (2019); <https://doi.org/10.1063/1.5089001>



Harmonic linearized Navier-Stokes equation on describing the effect of surface roughness on hypersonic boundary-layer transition

Cite as: Phys. Fluids 31, 034108 (2019); doi: 10.1063/1.5086912
Submitted: 25 December 2018 • Accepted: 28 February 2019 •
Published Online: 27 March 2019



Lei Zhao (赵磊),¹  Ming Dong (董明),^{2,3} and Yanguang Yang (杨彦广)^{1,a)} 

AFFILIATIONS

¹Hypervelocity Aerodynamics Institute, China Aerodynamics Research and Development Center, Mianyang 621000, China

²Department of Mechanics, Tianjin University, Tianjin 300072, China

³Laboratory for High-Speed Aerodynamics, School of Mechanical Engineering, Tianjin University, Tianjin 300072, China

^{a)}Electronic mail: yangyanguang@cardc.cn

ABSTRACT

Laminar-turbulent transition is crucially influenced by wall roughness. This paper develops a numerical approach based on the harmonic linearized Navier-Stokes (HLNS) equations to accommodate the scattering effect of the rapidly distorted mean flow induced by a two-dimensional hump or indentation at the wall on the oncoming instability modes (including the Mack first and second modes) in a hypersonic boundary layer. Due to the ellipticity of the scattering system when the roughness width is comparable with the instability wavelength, the traditional linear stability theory and the linear parabolized stability equation do not apply, and therefore, the HLNS approach has advantages in both accuracy and efficiency. The impact of a roughness is characterized by a transmission coefficient, which is the ratio of the asymptotic amplitude downstream of the roughness to that upstream. At a Mach number of 5.92, the dependence of the transmission coefficient on the frequency and the oblique angle of the oncoming mode and the size and location of the hump/indentation is studied systematically. It is confirmed that the synchronization frequency appears as a critical frequency, above and below which the oncoming instability modes are suppressed and enhanced by the roughness, respectively, which provides fundamental basis to the laminar-flow control in hypersonic boundary layers.

Published under license by AIP Publishing. <https://doi.org/10.1063/1.5086912>

I. INTRODUCTION

Laminar-turbulent transition in hypersonic boundary layers is of fundamental importance to the design of high-speed vehicles due to its direct relevance to a variety of issues such as lift, drag, and heat transfer. The wall roughness is always regarded as a crucial factor to influence the transition onset. Depending on the size of the roughness, the transition may be triggered through two different routes, i.e., the natural and bypass routes. As observed in early experiments on supersonic boundary layers (see Ref. 1), a low roughness only causes limited movement of the transition onset. However, when the roughness height is increased to some critical size, then the transition will move to the upstream direction apparently, and transition can be triggered immediately behind the roughness if the latter arrives at an “effective” size.^{2,3} Such observation is recently confirmed in quiet wind tunnels,^{4,5} indicating the dominant role played

by the roughness even when the background perturbation is almost absent. Recent work suggests that the roughness of the cone nose-tip also influences the laminar-turbulent transition at hypersonic speed.^{6,7}

It is well accepted that a three-dimensional (3-D) roughness element with moderate height would induce a pair of longitudinal streaks in its wake, which supports the so-called bi-global instability modes with high growth rates.^{8–10} The accumulation of the latter would trigger transition directly, bypassing the participation of the normal modes, e.g., the Tollmien-Schlichting (T-S) mode in the subsonic/incompressible regime¹¹ and the Mack modes in the hypersonic regime.¹² In this scenario, the laminar-turbulent transition is promoted remarkably and is referred to as the bypass transition.

However, for a low roughness, especially when the roughness is two-dimensional (2-D), transition in hypersonic boundary layers would be delayed in some circumstances, which is different

from the investigations in the subsonic regime.^{13–17} In Holloway and Sterrett's experiment,¹⁸ it was found that a roughness with a height lower than the local boundary-layer thickness did delay transition at oncoming Mach numbers 4.8 and 6.0. More recently, Fujii¹⁹ performed experiments on a hypersonic sharp-cone boundary layer with a 2-D roughness at Mach number 7.1, and the delay of transition was also observed. As a matter of fact, the boundary-layer transition in these configurations follows the natural route, which is attributed to the accumulation of the boundary-layer normal modes. The presence of the surface roughness induces a moderate mean-flow distortion that would promote or delay transition in the following two regimes: (i) The nonlinear interaction between the freestream perturbation and wall roughness would directly generate boundary-layer instability modes, which is referred to as the local receptivity problem. By combining the asymptotic and numerical techniques, Fedorov²⁰ formulated the local receptivity of the hypersonic Mack modes with the freestream perturbation appearing as acoustic waves. The key issue of the local receptivity process is essentially a modulation of the dispersion relation from the freestream perturbations to boundary-layer modes by the roughness-induced mean-flow distortion. In comparison with the leading-edge receptivity,^{21,22} in which the instability modes undergo a long-distance damping from the leading edge to its neutral position, the roughness-induced receptivity is often more efficient. (ii) The oncoming instability mode can be scattered by the roughness in a local area, leading to an increase or decrease of its asymptotic amplitude in the downstream limit. Accordingly, the transition location may be shifted due to the change of the amplitude accumulation. Based on the triple-deck formalism, Wu and Dong²³ developed a local scattering theory to accommodate the scattering of the oncoming T-S mode in the subsonic regime. In this theory, a transmission coefficient \mathcal{T} is introduced to characterize the ratio of the asymptotic amplitude downstream of the roughness to that upstream. It is a generic framework, and the mean-flow distortion can also be any other local abrupt change. Dong and Wu^{24,25} and Dong and Zhang²⁶ applied the local scattering framework to the scattering problems induced by suction/injection, trailing-edge and steps, respectively. If there are a series of isolated roughness elements, then the oncoming instability mode is scattered by each roughness individually, and so the downstream amplitude is shifted by a factor of $\prod_i \mathcal{T}_i$, where the subscript i denotes the index of the isolated roughness. This leads to a modified e^N method for transition prediction, i.e., in comparison with the smooth-wall case, the N -factor characterizing the amplification threshold of the perturbation should be decreased by ΔN , and the decrement $\Delta N = \sum_i \ln \mathcal{T}_i$; see Refs. 23 and 27–29. The second regime (scattering of the instability modes) is well understood in the subsonic or incompressible regimes, where the boundary-layer instability modes appear as a viscous T-S wave. On the other hand, the inviscid Mack (second) mode always plays a dominant role in the natural transition in hypersonic boundary layers and the scattering of the oncoming Mack modes by the local roughness is attributed to a different mechanism from that of the T-S wave. Since the perturbation profile of the Mack mode peaks in the main part of the boundary layer, the nonlinear interaction between the oncoming Mack modes and the wall roughness appears in the main layer, which is in contrast to the near-wall nature of the T-S wave. Therefore, in order to see a moderate scattering effect, the roughness needs to be higher than

the viscous sublayer. Additionally, the hypersonic first mode with a relatively small oblique angle (the ratio of the spanwise wavenumber to the streamwise wavenumber) also belongs to the inviscid regime.³⁰

In order to understand the underlying mechanism of the transition delay caused by a 2-D roughness in hypersonic boundary layers as observed by previous experiments, direct numerical simulations (DNSs) have been performed on the regime (ii) recently [because regime (i) can only promote transition]. Marxen *et al.*³¹ calculated the disturbance evolution in a Mach 4.8 boundary layer with 2-D roughness, and found that the roughness strongly enhances the growth of the unstable waves at a selected frequency range and a stabilizing effect appears when the frequency is even higher. Duan *et al.*³² and Fong *et al.*^{33,34} simulated the same problem by changing the oncoming Mach number to 5.92. Through a number of case studies for different roughness locations, they concluded that the synchronization frequency, denoting the intersection of the fast and slow modes,³⁵ acts as a critical frequency, above and below which the oncoming inviscid modes are suppressed and enhanced by the 2-D roughness, respectively. Note that under this oncoming condition, the unstable zones of the first and second modes merge, leading to the disappearance of the upper neutral point of the first mode and the lower neutral point of the second mode. Sawaya *et al.*³⁶ further studied the impact of a variety of wall imperfections, including the backward and forward steps, surface dips, surface humps, and wavy walls, on the development of hypersonic boundary-layer modes. In order to provide experimental verification on the role of the synchronization frequency, Fong *et al.*³⁷ designed a roughness distribution and an experiment for a flared cone at the Boeing/AFOSR Mach 6 quiet wind tunnel at Purdue University was conducted. A considerable suppression of the second mode is observed from the experiment. Tang *et al.*³⁸ experimentally investigated the development of second-mode instability in a Mach 6 flat-plate boundary layer with a 2-D roughness. It is found that the roughness has a limited impact on the perturbation amplitude in the downstream limit when the roughness is too narrow in comparison with the wavelength of the second mode.

Although the above DNS and experimental studies can provide us quantitative results on individual cases, reduced-order theories need to be developed to make the systematical study possible such that sufficient evidence to draw an overall picture on the scattering nature can be provided. As the non-parallelism of the Blasius solution is weak, the spatial growth rate obtained from the Orr-Sommerfeld (O-S) solution (under parallel-flow assumption) can be applied to predict the amplitude evolution of the normal modes on a smooth flat plate with limited error. However, the presence of surface roughness could induce a more significant mean-flow distortion locally, leading to a strong non-parallelism and the invalidity of the O-S equations. Thus, Park and Park³⁹ and Fong and Zhong⁴⁰ performed the linear parabolized stability equation (LPSE) to calculate the scattering of the oncoming Mack modes by local two-dimensional humps in hypersonic boundary layers. However, the parabolized approach can only accommodate the “weak” non-parallelism and is inapplicable when the roughness width is comparable with the wavelength of the oncoming modes because the problem is essentially elliptic, especially when a separation zone appears. A more reasonable approach is the so-called Harmonic Linearized Navier-Stokes (HLNS) equations, in which no artificial parabolized

restriction is introduced such that the elliptic nature of the governing equations is kept unchanged. Raposo *et al.*⁴¹ and Huang and Wu⁴² used the HLNS to study the receptivity and linear scattering problems in the subsonic/incompressible regime, respectively. In these studies, the oncoming instability modes are viscous T-S waves, with wavelengths of $O(Re^{-3/8}L)$,³⁰ where $Re \equiv U_\infty^* L/\nu$ is the Reynolds number with U_∞^* , L , and ν being the velocity of the oncoming stream, the distance between the roughness, and the leading edge and the kinematic viscosity, respectively. Since $Re \gg 1$, the wavelength is much longer than the local boundary-layer thickness $\delta = O(Re^{-1/2}L)$, and hence the roughness width is chosen to be larger than δ to satisfy the resonant condition. On the other hand, in hypersonic flows, only the first mode with very oblique angle and low frequency agrees with the viscous T-S mode,³⁰ and the instability modes, including the quasi-2-D first mode and all the second and higher-order modes, are of inviscid nature. As the inviscid modes have comparable wavelengths with the local boundary-layer thickness δ , the roughness width is chosen to be of $O(\delta)$. This paper will focus on this issue by developing the HLNS approach in the hypersonic regime.

II. MATHEMATICAL DESCRIPTION

A. Physical model

As sketched in Fig. 1(a), the physical model to be studied is a 2-D hypersonic (the supersonic regime can also be included) boundary-layer flow over a flat plate with an isolated surface roughness. The oncoming flow is assumed to be perfect gas, and the dynamic viscosity μ is assumed to satisfy Sutherland's law. The heat conductivity κ is related to μ via a constant Prandtl number ($Pr = 0.72$). A 2-D isolated roughness element, with a height lower than the boundary-layer thickness, is located at a distance L downstream of the leading edge. When an oncoming instability mode, e.g., the Mack first or second mode, propagates over the roughness, it would be scattered by the rapidly distorted mean flow, leading to a sudden change of its amplitude in the close neighbourhood of the roughness. Such change may affect the downstream amplitude accumulation, which would cause the promotion or delay of the laminar-turbulent

transition. The width of the roughness is comparable with the wavelength of the instability mode such that the scattering efficiency is moderate due to the resonance mechanism. Thus, the whole system is elliptic, and the traditional O-S and parabolized stability equations⁴³ do not apply anymore. Therefore, in order to accommodate the ellipticity, we are going to formulate a HLNS approach by assuming the amplitude of the oncoming mode to be infinitesimally small.

Both the Cartesian and body-fitted coordinate systems are utilized in this paper. The Cartesian coordinate (x^*, y^*, z^*) , with its origin locating at the leading edge, and the time t^* are normalized as

$$(x, y, z) = (x^*, y^*, z^*)/L \quad \text{and} \quad t = t^* U_\infty^*/L,$$

where U_∞^* denotes the velocity of the oncoming stream. In what follows, the subscript ∞ denotes the quantity of the oncoming flow and the asterisk denotes the dimensional quantity. The density, velocity field, temperature, and pressure are normalized by their oncoming quantities,

$$(\rho, u, v, w, T, p) = \left(\frac{\rho^*}{\rho_\infty^*}, \frac{u^*}{U_\infty^*}, \frac{v^*}{U_\infty^*}, \frac{w^*}{U_\infty^*}, \frac{T^*}{T_\infty^*}, \frac{p^*}{\rho_\infty^* U_\infty^{*2}} \right).$$

The oncoming Mach number Ma and the Reynolds number Re are defined as

$$Ma = U_\infty^*/a_\infty^*, \quad Re = \rho_\infty^* U_\infty^* L/\mu_\infty^*,$$

where a_∞^* and μ_∞^* represent the sound speed and the dynamic viscosity, respectively.

Note that, we are considering a boundary layer on a flat plate with a sharp leading edge, the oblique shock wave radiating from the leading edge is rather weak and the aforementioned "oncoming flow" represents the flow behind the weak leading-edge shock wave.

B. Harmonic linearized Navier-Stokes (HLNS) equations in the computational coordinate system

For simplicity, we denote $\phi \equiv (\rho, u, v, w, T)^T$. In general, the flow field can be decomposed as a superposition of a steady mean flow and an unsteady perturbation,

$$\phi(x, y, z, t) = \bar{\phi}(x, y) + \phi'(x, y, z, t), \quad (1)$$

where the overbar and prime represent the quantities of the mean flow and perturbation, respectively.

1. Mean flow and instability modes

The mean flow is obtained by using an in-house Navier-Stokes solver, as used in Refs. 44 and 45. We select the no-slip ($u_s = w_s = 0$), non-penetration ($v_s = 0$), and isothermal ($T_s = T_w$) conditions at the wall, where the subscript "s" represents the quantities at the wall, $T_w \equiv T_w^*/T_\infty^*$ is fixed beforehand. The outflow condition is selected at the upper boundary. Since the roughness is 2-D, the mean quantities $\bar{\phi}$ are functions of x and y only. If the inflow boundary of the computational domain is chosen to be sufficiently upstream of the roughness, then the mean flow at the inlet satisfies the unperturbed similarity solution of compressible laminar boundary layers⁴⁶ approximately. As the neighbourhood of the roughness is approached, the mean flow deviates the similarity solution significantly and the distortion acts as the seeds to promote scattering of

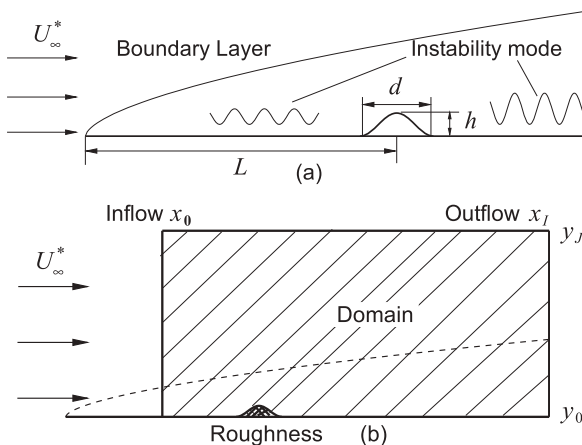


FIG. 1. Sketches of the physical model (a) and computational domain (b).

the oncoming instability modes. In the downstream limit, the velocity field tends to recover to the unperturbed state, and the outflow condition is imposed. Note that the upstream similarity solution profile (of course with a certain stretch due to the development of the boundary-layer thickness) may not be recovered if a strong shock is induced by a sufficiently high roughness because the Mach number at the edge of the boundary layer is reduced. However, in the case studies of this paper, the impact of the shock is never significant as will be verified in Sec. III B.

Assume that the perturbation is sufficiently small in amplitude, and so its evolution can be described by the linearized Navier-Stokes equation. In both the upstream and downstream limits, since $\partial \bar{u}/\partial x$ and \bar{v} are small, the parallel-flow assumption is a good approximation. Therefore, the perturbation is expressed as a travelling-wave form

$$\phi'(x, y, z, t) = \epsilon \hat{\phi}(y) e^{i(\alpha x + \beta z - \omega t)} + c.c., \quad (2)$$

where, for spatial mode, the real numbers ω and β represent the radian frequency and the spanwise wavenumber, respectively, α and $\hat{\phi}(y)$ represent the complex streamwise wavenumber and the eigenfunction, respectively, $\epsilon \ll 1$ denotes the amplitude, and *c.c.* denotes the complex conjugate. Substituting (2) into the linearized Navier-Stokes equations and neglecting the small terms associating with the non-parallelism lead to the O-S equations. Imposing the homogeneous boundary conditions, we can obtain the discrete-mode solutions by the numerical method of Malik.⁴⁷

2. Governing equations of the infinitesimal perturbation

Since the roughness shifts the wall surface from a straight line to a locally bent curve, it is better to transform the Cartesian system (x, y, z) into a body-fitted coordinate system (ξ, η, z) , where $\eta = 0$ represents the wall. The relation between the two coordinate systems is

$$\xi_x = Jy_\eta, \quad \eta_x = -Jy_\xi, \quad \xi_y = -Jx_\eta, \quad \eta_y = Jx_\xi, \quad (3)$$

where the Jacobian determinant

$$J = \left| \frac{\partial(x, y)}{\partial(\xi, \eta)} \right|^{-1}. \quad (4)$$

Substitute (1) into the Navier-Stokes equations and subtract the mean equations out, then we arrive at the governing equations of the infinitesimal perturbation,

$$\begin{aligned} &(\Gamma \frac{\partial}{\partial t} + \bar{A} \frac{\partial}{\partial \xi} + \bar{B} \frac{\partial}{\partial \eta} + \bar{C} \frac{\partial}{\partial z} + \bar{D} + V_{\xi\xi} \frac{\partial^2}{\partial \xi^2} + V_{\eta\eta} \frac{\partial^2}{\partial \eta^2} + V_{zz} \frac{\partial^2}{\partial z^2} \\ &+ V_{\xi\eta} \frac{\partial^2}{\partial \xi \partial \eta} + V_{\xi z} \frac{\partial^2}{\partial \xi \partial z} + V_{\eta z} \frac{\partial^2}{\partial \eta \partial z}) \phi'(\xi, \eta, z, t) = 0, \end{aligned} \quad (5)$$

where coefficient matrices $\Gamma, \bar{A}, \bar{B}, \bar{C}, \bar{D}, V_{\xi\xi}, V_{\eta\eta}, V_{zz}, V_{\xi\eta}, V_{\xi z}$, and $V_{\eta z}$ are functions of the mean quantities, as illustrated in Appendix A.

3. HLNS equations

The spatially evolving perturbations are periodic in time and the spanwise direction, but growing in the streamwise direction. If the perturbation is Fourier transformed in t and z , then each

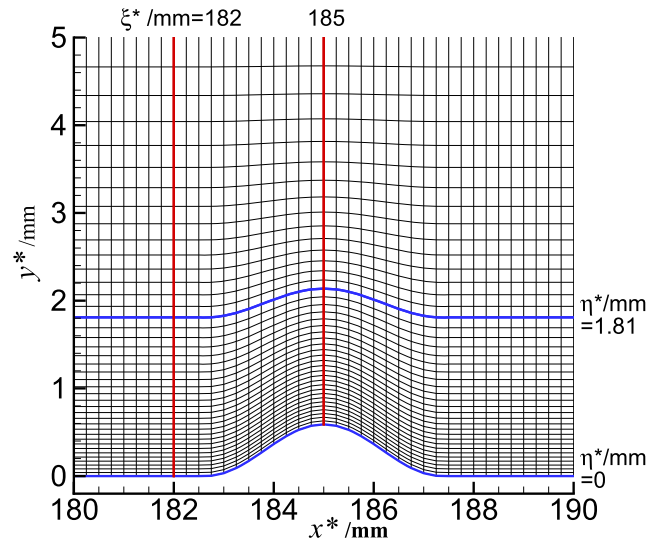


FIG. 2. Mesh near the roughness, where only one out of five vertical grid points is plotted. The red and blue lines denote the body-fitted coordinates (ξ, η) .

Fourier mode evolves like $\exp[i(\beta z - \omega t)]$, where β and ω denote the spanwise wavenumber and radian frequency, respectively. In the upstream and downstream limits, the dependence of the perturbation on x is separated into two parts, i.e., a fast one and a slow one. The former grows like $\exp(i\alpha x)$ (note that at the smooth surface away from the roughness, ξ and x are the same as shown in Fig. 2), where $\alpha = \alpha_r + i\alpha_i$ is complex with its real and imaginary parts representing the streamwise wavenumber and damping rate (inverse of the growth rate), respectively, while the latter modulates the amplitude gently due to the weak non-parallel mean profile. However, in the vicinity of the roughness that has a comparable width with the instability-mode wavelength, the slow part becomes fast as well because the non-parallelism of the mean-flow distortion is so significant that the perturbation does not behave as a traveling wave any more. In the HLNS approach, we express the perturbation field at a given frequency-spanwise-wavenumber $(\omega - \beta)$ space as

$$\phi'(\xi, \eta, z, t) = \epsilon \tilde{\phi}(\xi, \eta) e^{i(\alpha_0 \xi + \beta z - \omega t)} + c.c., \quad (6)$$

where α_0 is a reference complex wavenumber and $\tilde{\phi}(\xi, \eta)$ represents the shape function of the perturbation at a location ξ . In comparison with the traveling-wave form (2), the variation of the perturbation profile with ξ is allowed in (6). The reference wavenumber α_0 is simply selected as the eigen-solution of the O-S equations by setting the base flow as the similarity solution at $\xi = x_0$.

Substituting (6) into (5) yields the HLNS equations,

$$(\tilde{D} + \tilde{A} \frac{\partial}{\partial \xi} + \tilde{B} \frac{\partial}{\partial \eta} + V_{\xi\xi} \frac{\partial^2}{\partial \xi^2} + V_{\eta\eta} \frac{\partial^2}{\partial \eta^2} + V_{\xi\eta} \frac{\partial^2}{\partial \xi \partial \eta}) \tilde{\phi}(\xi, \eta) = 0. \quad (7)$$

The coefficient matrices \tilde{A}, \tilde{B} , and \tilde{D} are given by

$$\begin{aligned} \tilde{A} &= \bar{A} + 2i\alpha_0 V_{\xi\xi} + i\beta V_{\xi z}, & \tilde{B} &= \bar{B} + i\alpha_0 V_{\xi\eta} + i\beta V_{\eta z}, \\ \tilde{D} &= \bar{D} - i\omega\Gamma + i\alpha_0 \bar{A} + i\beta \bar{C} - \alpha_0^2 V_{\xi\xi} - \beta^2 V_{zz} - \alpha_0 \beta V_{\xi z}. \end{aligned}$$

4. Discretization

The HLNS equations are discretized in a computational domain $\xi \in [x_0, x_I]$ and $\eta \in [0, y_I]$ ($y \in [y_0, y_I]$), as shown in Fig. 1(b), and the numbers of the grid points are $I + 1$ and $J + 1$ in the streamwise and wall-normal directions, respectively.

At the wall, the no-slip, non-penetration, and isothermal conditions are imposed,

$$\tilde{u} = \tilde{v} = \tilde{w} = \tilde{T} = 0, \quad \text{at } \eta = 0. \quad (8)$$

Since the perturbation damps exponentially in the far field, we have

$$\tilde{\phi} = 0 \quad \text{at } \eta = y_I, \quad (9)$$

provided that y_I is sufficiently large. At the inflow $\xi = x_0$, because the non-parallelism is negligible, the perturbation is described by the solution of the O-S equation,

$$\tilde{\phi}(x_0, y) = \hat{\phi}(y). \quad (10)$$

If the outlet of the computational domain $\xi = x_I$ is located sufficiently downstream from the scatter, then the perturbation quantities at the outlet can be fully determined by the immediately upstream information, despite the ellipticity of the HLNS equations. Therefore, an outflow condition is imposed here, i.e., a unilateral difference scheme is used to discretize the partial derivatives $\partial/\partial\xi$, $\partial^2/\partial\xi^2$, and $\partial^2/(\partial\xi\partial\eta)$ in the ξ direction.

The partial derivatives of $\tilde{\phi}$, i.e., $\partial/\partial\xi$, $\partial/\partial\eta$, $\partial^2/\partial\xi^2$, $\partial^2/\partial\eta^2$, and $\partial^2/(\partial\xi\partial\eta)$, are discretized by using five-point finite-difference schemes with fourth-order accuracy, as illustrated in Appendix B. Note that for points near the boundary of the computational domain, where the standard difference stencils include some points outside the domain, we move the stencils inward accordingly instead of reducing the accuracy of the difference schemes. Being different from the LPSE, Eq. (7) is an elliptic system that has two advantages: (i) the numerical instability appearing in PSE is avoided, and more importantly, and (ii) it agrees with the physical nature when the roughness has a comparable width with the instability-mode-wavelength.

Discretization ultimately yields a system of algebraic equations of a generic form,

$$\mathbf{M}\tilde{\mathbf{q}} = \tilde{\mathbf{r}}, \quad (11)$$

where \mathbf{M} is a $5(I + 1)(J + 1) \times 5(I + 1)(J + 1)$ dimensional matrix,

$$\tilde{\mathbf{q}} = (\tilde{\phi}_{0,0}, \dots, \tilde{\phi}_{0,j}, \dots, \tilde{\phi}_{0,J}, \dots, \tilde{\phi}_{i,0}, \dots, \tilde{\phi}_{i,j}, \dots, \tilde{\phi}_{i,J}, \dots, \tilde{\phi}_{I,0}, \dots, \tilde{\phi}_{I,j}, \dots, \tilde{\phi}_{I,J})$$

is a $5(I + 1)(J + 1)$ dimensional vector including all the physical quantities in the computational domain, and vector $\tilde{\mathbf{r}}$ is the inhomogeneous forcing of the linear system that imposes the inflow condition.

The Direct Sparse Solver (DSS) provided by the Intel Math Kernel Library (MKL) is employed to solve the system of sparse algebraic equation (11).

C. Quantitative description of the scattering effect

Following Wu and Dong,²³ we introduce a transmission coefficient \mathcal{T} , which is defined as the ratio of the asymptotic amplitude of

the instability mode downstream of the roughness to that upstream, i.e.,

$$\mathcal{T} = \lim_{x \rightarrow \infty} A(x)/A_0(x), \quad (12)$$

where A_0 and A represent the amplitude of the instability mode without and with the roughness, respectively. Since the wake of the roughness damps algebraically along x , the mean flow tends to recover to the unperturbed similarity solution. Therefore, in the downstream limit, $A(x)/A_0(x)$ approaches a real constant \mathcal{T} . If $\mathcal{T} > 1$, then the roughness acts as an amplifier that enhances the oncoming instability mode, while $\mathcal{T} < 1$ implies the stabilizing effect of the roughness.

III. NUMERICAL RESULTS

A. Flow configurations

As case studies, we choose the flow parameters according to the numerical investigations performed by Fong *et al.*,^{33,34} and the oncoming Mach number, the unit Reynolds number $Re_u \equiv \rho_\infty^* U_\infty^* / \mu_\infty^*$, the freestream and wall temperatures are shown in Table I. As shown in Table II, three Reynolds numbers $Re \equiv Re_u L$ are considered and the corresponding boundary-layer thickness δ_{99} is also exhibited.

The surface roughness is assumed to be a cosine shape,

$$F(x^*) = \begin{cases} \frac{h}{2} \left\{ 1 + \cos \left[\frac{2\pi}{d} (x^* - L) \right] \right\}, & \text{if } |x^* - L| \leq d/2, \\ 0, & \text{if } |x^* - L| > d/2, \end{cases} \quad (13)$$

where h and d denote the height and width of roughness, respectively. The roughness appears as a hump for $h > 0$ and an indentation for $h < 0$. In order to study the impact of the roughness shape on the instability modes, we choose the Re (or L) from case 1 in Table II as a typical setup and vary the height of the hump (cases 1.1-1.5), the depth of the indentation (cases 1.6-1.10), and the width of the hump (cases 1.5 and 1.11-1.13), as shown in Table III. In addition, the dependence of the scattering effect on the Reynolds number is considered by comparing cases 1.5, 2.5, and 3.5.

For each case in Table II, the computational domain is selected as $[x_0^*, x_I^*] \times [y_0^*(x^*), y_I^*]$, where x_0^* and x_I^* are shown, $y_0^*(x^*) = F(x^*)$ and $y_I^* = 200$ mm. Uniform mesh is employed in the x^* direction, while non-uniform mesh that is clustered in the near-wall

TABLE I. Parameters of oncoming flow.

Ma	Re_u	T_∞^*	T_w^*
5.92	$1.32 \times 10^7/\text{m}$	48.69 K	334.9 K

TABLE II. Parameters related to different roughness locations.

	L (mm)	Re	δ_{99} (mm)	x_0^* (mm)	x_I^* (mm)	f_s (kHz)
Case 1	185	2.442×10^6	2.36	100	400	128.5
Case 2	330	4.356×10^6	3.15	250	550	95.0
Case 3	410	5.412×10^6	3.51	330	630	84.9

TABLE III. Parameters related to roughness size.

	L (mm)	d/δ_{99}	h/δ_{99}		L (mm)	d/δ_{99}	h/δ_{99}
Case 1.1	185	2	0.05	Case 1.6	185	2	-0.25
Case 1.2	185	2	0.10	Case 1.7	185	2	-0.30
Case 1.3	185	2	0.15	Case 1.8	185	2	-0.35
Case 1.4	185	2	0.20	Case 1.9	185	2	-0.40
Case 1.5	185	2	0.25	Case 1.10	185	2	-0.50
Case 1.11	185	4	0.25	Case 2.5	330	2	0.25
Case 1.12	185	6	0.25	Case 3.5	410	2	0.25
Case 1.13	185	8	0.25	Case 1.0	185	0	0

region is employed in the y^* direction. For the current calculation, we select $I = 1200$ and $J = 300$. As a matter of fact, the HLNS equations can be solved in any smooth mesh system, and in this paper, we allocate the grid points by the following means, i.e.:

$$x_{ij}^* = x_0^* + (x_I^* - x_0^*)i/I, \quad y_{ij}^* = \bar{y}_j^* + F(x^*)e^{-(\bar{y}_j^*/\delta_{99})^2},$$

where the subscripts $i \in [0, I]$ and $j \in [0, J]$ denote the index of the grid points in the streamwise and wall-normal directions, respectively, and

$$\bar{y}_j^*/\delta_{99} = \frac{aj/J}{1 + a/\bar{y}_j - j/J}, \quad a = \frac{\bar{y}_j}{\bar{y}_j - 2}, \quad \bar{y}_j = y_j^*/\delta_{99}.$$

The above distribution guarantees that half of the grid points are allocated in the range of $[0, \delta_{99}]$. Figure 2 plots the mesh system near the roughness, where only one out of five grid points in the vertical direction is shown. As a mapping from the Cartesian system to the body-fitted one, we simply take $\xi_i^* = x_{i,0}^*$ and $\eta_j^* = y_{0,j}^*$.

B. Mean flow distorted by roughness

By using the DNS solver, we are able to obtain the mean flow roughness-distorted. Figure 3 displays the streamwise distributions of the pressure $\bar{p}(x^*, y_0^*)$ and the mean shear $\partial \bar{u}/\partial y^*(x^*, y_0^*)$ at the wall for different roughness heights (cases 1.1, 1.3, 1.5, and 1.6) with fixed roughness width $d/\delta_{99} = 2$ and location $L = 185$ mm ($Re = 2.442 \times 10^6$). In the locations upstream of the roughness, a hump produces a smooth adverse pressure gradient, which is followed by a region of a strong favorable pressure gradient in the vicinity of the roughness center. In the wake of the hump, the adverse pressure gradient is seen again and it approaches zero smoothly in the downstream limit. At a given streamwise location, a higher hump produces a stronger pressure gradient. The distribution of the pressure gradient induced by an indentation behaves inversely, and its intensity is much weaker

than that by a hump with the same height. The streamwise distributions of the surface mean shear for the same cases are shown in Fig. 3(b). A drastic increase of the mean shear is observed for hump cases, and the mean shear valleys are near both the leading ($x^* \approx 183$ mm) and trailing ($x^* \approx 187$ mm) edges of the humps. For $h/\delta_{99} = 0.25$ (case 1.5), the minimum value of the surface shear is slightly negative, which appears near the trailing edge of the hump. This indicates that a marginal separation zone is induced by the strong adverse pressure gradient, and further increasing the hump height will lead to an additional separation zone near its leading edge. On the contrary, a large separation zone appears inside the indentation for $h/\delta_{99} = -0.25$ (case 1.6).

The contours of the mean pressure are plotted in Fig. 4 for the four cases, as shown in Fig. 3. For the hump cases [Figs. 4(a)–4(c)], the red zone of the pressure contour illustrates the compression wave followed by the expansion wave (the blue zone). For the indentation case [Fig. 4(d)], the expansion wave is followed by the compression wave. As the hump height increases, the level of the pressure peak increases. Also shown in the figures are the streamlines, and the bent streamlines reflect the distortion of the mean flow by the roughness. A tiny separation zone appears at the trailing edge of the hump for case 1.5, and a large separation zone almost possesses the whole indentation for case 1.6. Figure 5 displays the profiles of the mean streamwise velocity \bar{u} at different streamwise locations for case 1.5, and the similarity solution is also plotted for comparison at each position. Upstream of $x^* = 160$ mm, the mean flow satisfies the unperturbed similarity solution. An apparent distortion appears at the roughness, which leads to a shaper wall shear. The mean flow tends to recover to the similarity solution in the downstream limit ($x^* > 200$ mm). The downstream oblique shock induced by the surface roughness is rather weak that the Mach number at the edge does not change apparently.

C. Instability of the hypersonic boundary-layer modes

In order to determine the frequencies of our interests, we first analyze the instability modes in a hypersonic boundary layer over a smooth plate by solving the O-S equations. The dependence of the phase speed c_r and the growth rate $-\alpha_i^*$ of the two-dimensional ($\beta = 0$) instability modes on the frequency $f = (\omega U_\infty^*)/(2\pi L)$ is plotted in Fig. 6, where $Re = 2.442 \times 10^6$. Two types of discrete modes are found, which, according to Fedorov,³⁵ are termed as the fast mode (mode F) and the slow mode (mode S), respectively. As shown in Fig. 6(a), as $f \rightarrow 0$, the phase velocities of the fast and slow modes approach those of the fast ($c = 1 + 1/Ma$) and slow ($c = 1 - 1/Ma$) acoustic waves, respectively, which implies that the two boundary-layer modes synchronize with the freestream acoustic waves in the low-frequency limit. A similar picture is also seen

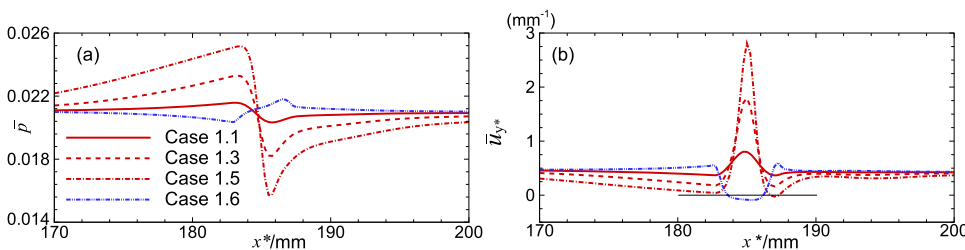


FIG. 3. The mean pressure $\bar{p}(x^*, y_0^*)$ (a) and the mean shear $\bar{u}_{y^*}(x^*, y_0^*)$ (b) at the wall for cases 1.1, 1.3, 1.5, and 1.6. The thin line in (b) represents the zero-shear line.

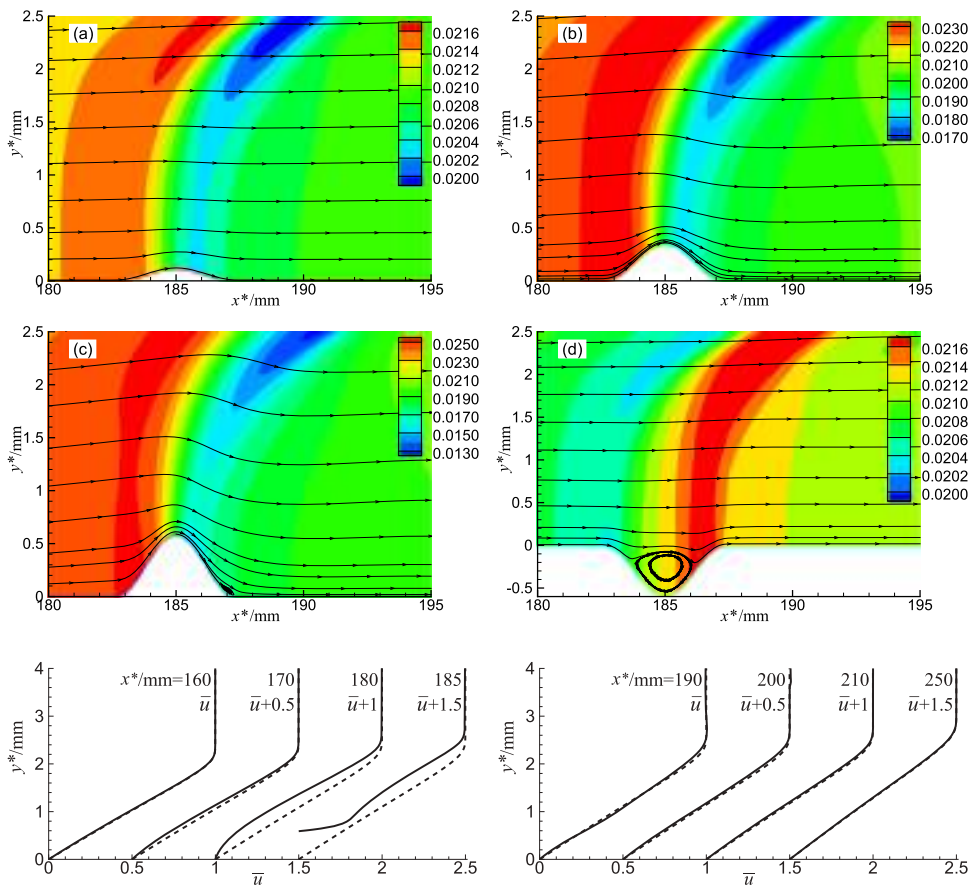


FIG. 4. The contours of $\bar{p}(x^*, y^*)$ and the streamlines for a hump (or an indentation) with $L = 185$ mm, $d/\delta_{99} = 2$, and different heights $h/\delta_{99} = 0.05$ (a), 0.15 (b), 0.25 (c), and -0.25 (d).

FIG. 5. Mean velocity profiles at different locations for case 1.5 (solid lines), where the dashed lines are for the similarity solution.

in the c_r - x plot by fixing the frequency at a certain value, and the implication is that mode F/S can be excited by the fast/slow acoustic wave from the leading edge of the plate. As f increases, c_r of mode F decreases, while that of mode S increases. The two modes intersect at $f_s \approx 128.5$ kHz, as marked by the vertical dashed lines, where f_s is recognized as the synchronization frequency of the two modes. As a matter of fact, the definition of the synchronization as defined by Fedorov²¹ and Fedorov and Tumin⁴⁸ is that both the real and imaginary parts of the wavenumber or phase speed should be equal. However, in most of the cases including the current one, the two conditions are not satisfied simultaneously. As shown in Fig. 6(b), the growth rates of the two modes are separated, and a certain difference is observed at f_s . Since the imaginary part of c or α is small, we approximately apply the concept of synchronization here, which is also the cases of Fong *et al.*^{33,34} As was pointed out by Fong *et al.*,^{33,34} the synchronization frequency may appear as a critical frequency that separates the impact of the roughness in two ranges, i.e., for frequencies lower than this critical value, the roughness plays a destabilizing role, while the roughness suppresses the oncoming instability mode for supercritical frequencies. The synchronization frequencies of modes F and S at the three Reynolds numbers, or locations of the roughness, are displayed in Table II. The plot of the growth rate in Fig. 6(b) also shows that the mode-F perturbations are always stable ($-\alpha_i^* < 0$) and mode-S perturbations are unstable ($-\alpha_i^* > 0$) in the frequency range of our interests

(10–200 kHz). By following the same analysis, we obtain that for $Re = 4.356 \times 10^6$ and 5.412×10^6 ($L = 330$ and 410 mm), the frequency ranges that we are interested in are 20–180 kHz and 20–160 kHz, respectively.

Additionally, Fig. 6(b) shows that the growth-rate curve of mode S has two peaks, which corresponds to the Mack first and second modes, as described by Mack.¹² Actually, a supersonic boundary layer supports a multiplicity of instability modes, and for $Ma > 4$, both the Mack first and second modes are usually unstable. In the current study, the upper branch of the former and the lower branch of the latter merge together, and we denote the frequency ($f_c = 96$ kHz) corresponding to the minimum growth rate between the two peaks as the interface of the two modes, which is marked by the vertical solid lines in Fig. 6.

Note that the 2-D second modes are always more unstable than the 3-D ones with the same frequencies, but the most unstable first mode is 3-D. The following calculations are for 2-D cases ($\beta = 0$) except in Fig. 14, where the impact of the spanwise wavenumber β is considered.

D. Validation of the HLNS approach and comparison with the LPSE approach

In order to verify the accuracy of the HLNS approach, we perform DNS on the evolution of the instability modes with three

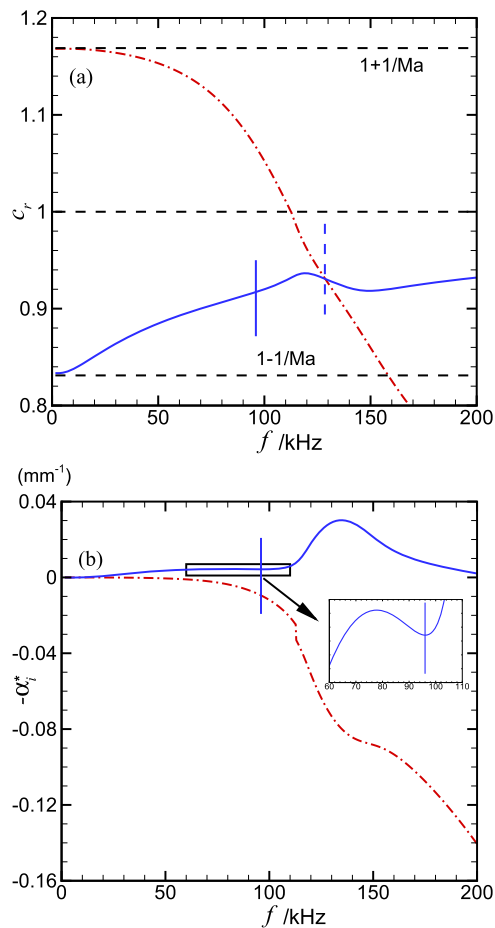


FIG. 6. The phase speed (a) and growth rates (b) of mode F (red dashed-dotted lines) and mode S (blue solid lines) versus the frequency for $Re = 2.442 \times 10^6$ and $\beta = 0$. In (a), the three horizontal dashed lines represent the $c = 1 + 1/Ma$, $c = 1$, and $c = 1 - 1/Ma$, respectively, and the vertical solid and dashed lines represent f_c and f_s , respectively.

typical frequencies, i.e., $f = 20$ kHz, 70 kHz, and 140 kHz, over a hump of case 1.5. The first two belong to the first mode, while the third one is the Mack second mode. The results of the streamwise evolution of the surface pressure fluctuations are compared with the HLNS approach, as shown in Fig. 7. The perturbations grow exponentially except in the close neighbourhood of the hump, where the apparent scattering effect is exhibited. Encouragingly, the curves from the two approaches overlap precisely for the whole frequency range, which confirms the reliability of our HLNS solver. Therefore, as an effective approach, the HLNS can be as accurate as the DNS approach on computing the evolution of linear perturbations, but the computational cost is much lower.

As illustrated in Sec. I, the LPSE is also an effective approach to investigate the distortion of the boundary-layer modes by surface roughness, but it is not applicable if the width of moderate roughness is comparable with the instability-mode wavelength (resonance regime). We therefore show the superiority of the HLNS to the LPSE

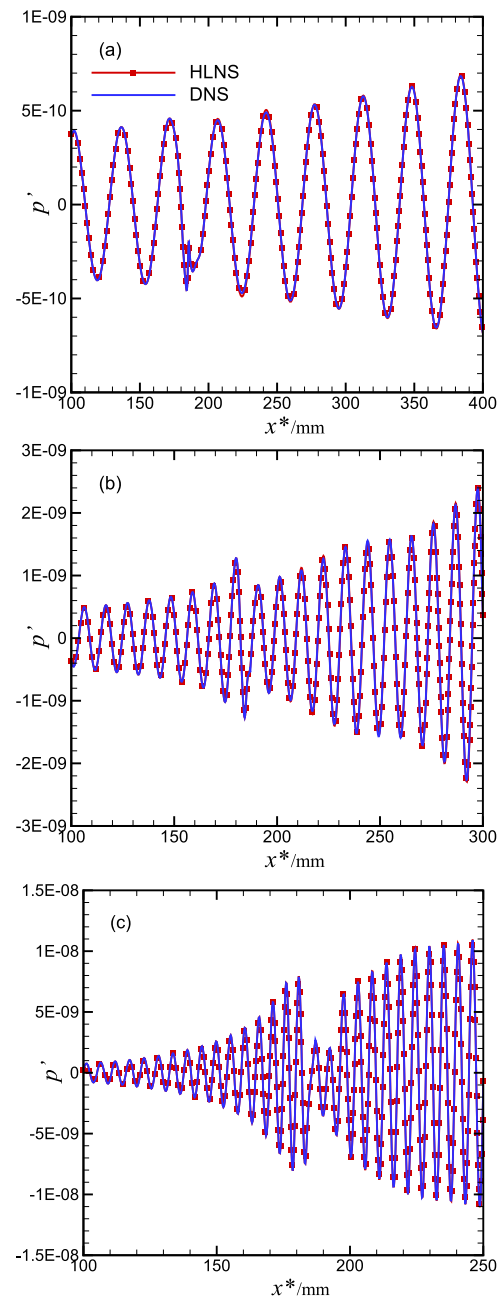


FIG. 7. Comparison of surface pressure fluctuations as obtained by HLNS (red symbolized lines) and DNS (blue lines) approaches for case 1.5, where $f = 20$ kHz (a), 70 kHz (b), and 140 kHz (c).

under the resonance configurations. The main difference between the LPSE and HLNS approaches is whether the elliptic term $\partial^2/\partial\xi^2$ is included. Based on the computational coordinate system (ξ, η) , if we replace the constant α_0 in Eq. (7) by $\alpha = \alpha(\xi)$, neglect the term $V_{\xi\xi}\partial^2/\partial\xi^2$, and add $ida/d\xi V_{\xi\xi}$ in the matrix \tilde{D} , then the system is parabolized, which is referred to as the LPSE. Note that in this

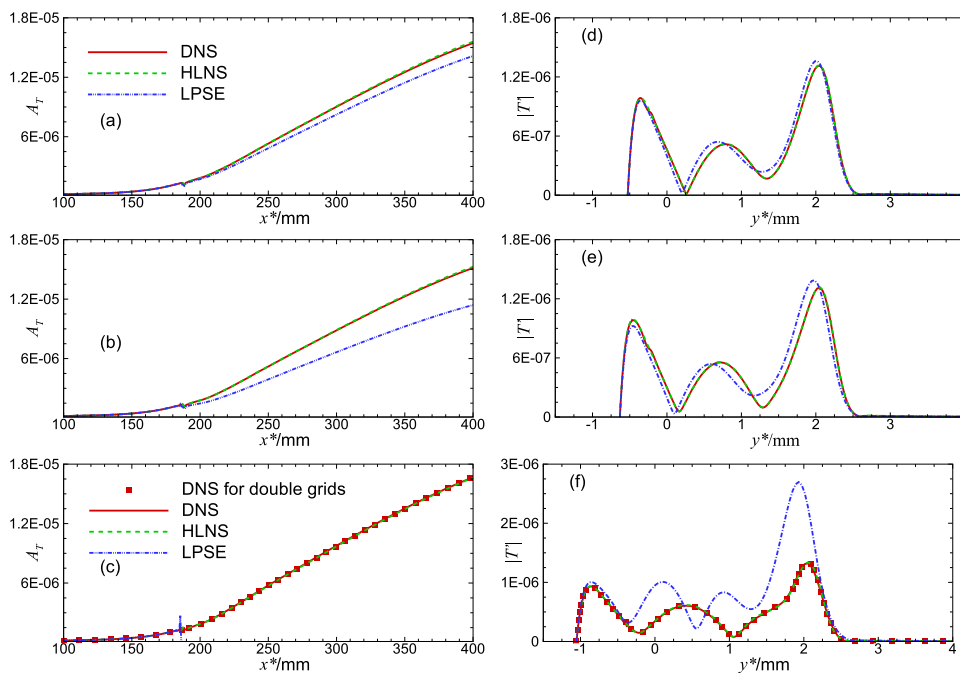


FIG. 8. Comparisons of the amplitudes of the temperature fluctuations [(a)–(c)] and the vertical profiles of the temperature perturbation at the location $x^* = 185.5$ mm [(d)–(f)] obtained by DNS, HLNS, and LPSE approaches for case 1.6 [(a) and (d)], case 1.7 [(b) and (e)], and case 1.10 [(c) and (f)] with $f = 140$ kHz. The DNS results for a refined mesh with double grid points in the x direction are also plotted in [(c) and (f)] for case 1.10.

calculation, the transverse coordinate η is not restricted to be perpendicular to the roughness surface. Such an approach is essentially the same as that of Park *et al.*^{39,43} A special effort has been devoted to alleviating the numerical instability that is caused by the remanent ellipticity of LPSE by following Chang *et al.*⁴⁹

We have carried out calculations by using the three approaches (DNS, HLNS, and LPSE) for cases 1.1–1.10. It has been found that the discrepancy between the HLNS and LPSE calculations is larger when the roughness appears as an indentation because the large separation zone appearing inside the indentation as shown in Fig. 4 may induce stronger ellipticity. Therefore, we plot the comparisons of the perturbation amplitude A_T and profiles $T'|_{x^*=185.5 \text{ mm}}$ as obtained from the three calculations for cases 1.6, 1.7, and 1.10 in Fig. 8. The frequency is selected to be $f = 140$ kHz (second mode), which induces a moderate scattering effect. For all the plots, the DNS and HLNS results are on top of each other, while the LPSE only provides a poor prediction for both the perturbation amplitude and its wall-normal profile. The accuracy of LPSE is lower for a deeper indentation, and for the deepest case 1.10, the LPSE calculation becomes divergent at $x^* = 186.25$ mm. In order to avoid the divergence, we have tried different grid spacings, but no improvement is obtained. Note that, for the moderate height hump cases, the perturbation profiles predicted by LPSE in the vicinity of the hump are never correct as well, although its prediction on the overall amplitude evolution in the downstream limit is reasonable. In addition, an increase of the hump height leads to a worse prediction. Therefore, we cannot trust the LPSE prediction for the moderate height hump cases because the agreement to the DNS results in the downstream limit appears by chance. The above comparison exhibits clearly the advantage of the HLNS on accommodating the elliptic scattering problem. Note that, for case 1.10 (the deepest indentation), the DNS results for the standard mesh agree well with those for the refined mesh with double

grid points in the x direction, which suggests that the grid points in the x direction are enough for the indentation cases. The resolution study for the HLNS approach is also performed; see Appendix C.

Additionally, since the mean flow for indentation cases exhibits inflectional points near the separation zone, some Kelvin-Helmholtz (K-H) instability may appear. However, they could at most appear in a restricted streamwise region since the mean flow recovers to the unperturbed similarity solution in the downstream limit. Therefore, from the viewpoint of transition prediction, we do not discuss the K-H mode in detail and only focus on the amplitude of the oncoming boundary-layer mode in the downstream limit.

E. Scattering effect of the roughness on hypersonic boundary-layer modes

By using the HLNS approach, we calculate the streamwise evolution of the instability modes for four typical frequencies (100 kHz, 115 kHz, 130 kHz, and 145 kHz) for case 1.5. The first two frequencies are sub-synchronization, the third one is very close to the synchronization frequency, and the last one is super-synchronization. The amplitudes of the temperature fluctuations A_T are shown as the red solid lines in Fig. 9. Note that the amplitudes of other quantities can lead to the same conclusion. In the upstream limit, the amplitude evolution agrees with that of the smooth-plate case (without roughness) as shown by the blue dashed-dotted lines. In the vicinity of the roughness $x^* \approx 185$ mm, the amplitude exhibits a kink, indicating the rapid deformation of the perturbation field. Up to a sufficiently downstream location (about $x^* = 250$ mm), the amplitude recovers to a smooth-evolution state, which agrees with a shifted version of that of the smooth plate case (blue dashed lines). The shifting factor depends on the frequency of the instability modes, i.e., for a relatively low frequency ($f = 100$ and 115 kHz), the factor is greater

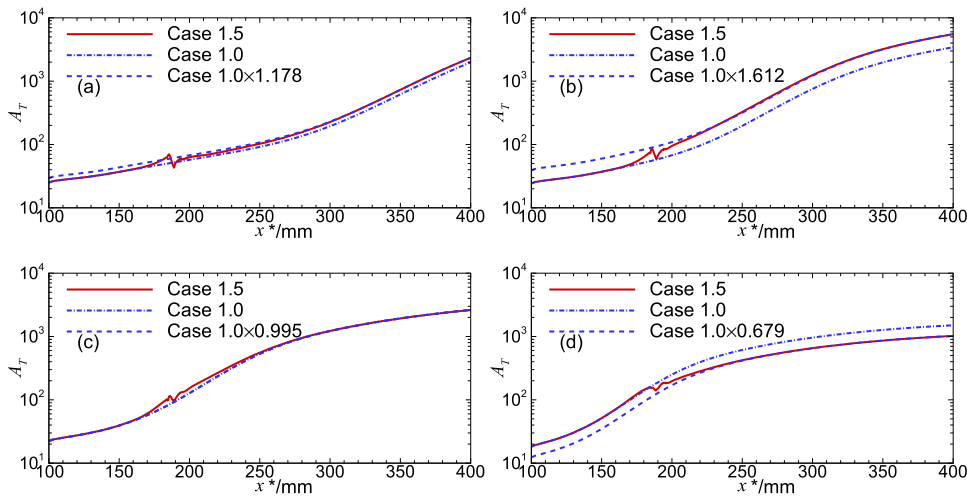


FIG. 9. Amplitude-evolution of the temperature fluctuations for case 1.5 (red lines) and case 1.0 (blue dashed-dotted lines) at frequencies of $f = 100$ kHz (a), 115 kHz (b), 130 kHz (c), and 145 kHz (d), where the dashed lines are a shift of the blue dashed-dotted lines by a factor of \mathcal{S} .

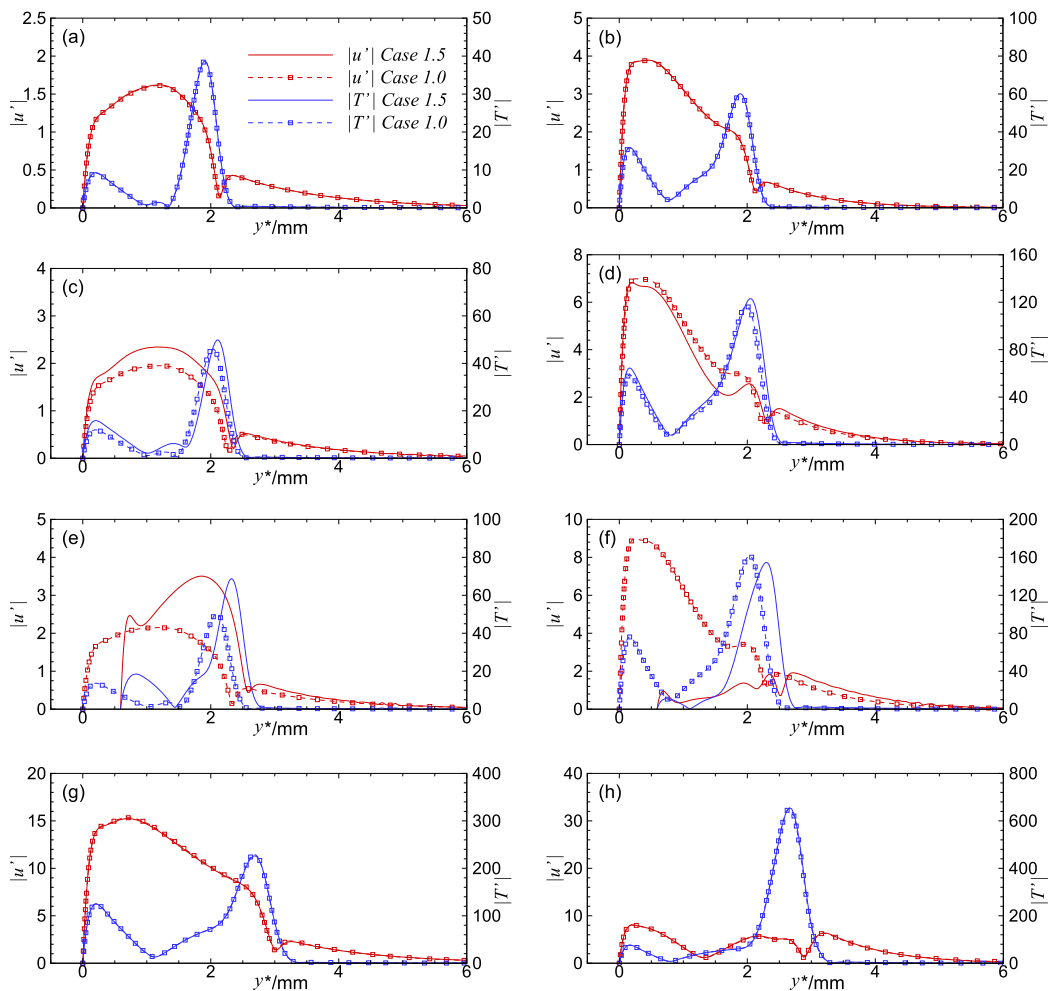


FIG. 10. Comparison of the perturbation profiles of u' and T' between cases 1.5 and 1.0. [(a) and (b)], [(c) and (d)], [(e) and (f)], and [(g) and (h)] are for $x^* = 155, 175, 185$, and 300 mm, respectively. [(a), (c), (e), and (g)] are for 100 kHz and [(b), (d), (f), and (h)] are for 145 kHz. In (g) and (h), the eigen-profiles for case 1.0 are multiplied by a factor \mathcal{S} .

than unity, implying a destabilizing effect; while for a high frequency $f = 145$ kHz, the impact of the roughness is stabilizing. A rather weak scattering effect is observed for the quasi-synchronization frequency $f = 130$ kHz since the shifting factor is approximately unity. The shifting factor is essentially the transmission coefficient \mathcal{T} as defined previously. The above observations agree with Marxen *et al.*³¹ and Fong *et al.*^{33,34} qualitatively.

Figure 10 compares the perturbation profiles of u' and T' at different x^* between cases 1.5 and 1.0 (with and without roughness). Two typical frequencies $f = 100$ and 145 KHz are selected, which correspond to the sub- and super-synchronization frequencies, respectively. At sufficiently upstream positions, e.g., $x^* = 155$ mm, the perturbation profiles for the two cases agree well with each other, indicating a rather weak impact of the roughness in the upstream limit. This also agrees with the feature of the amplitude evolution,

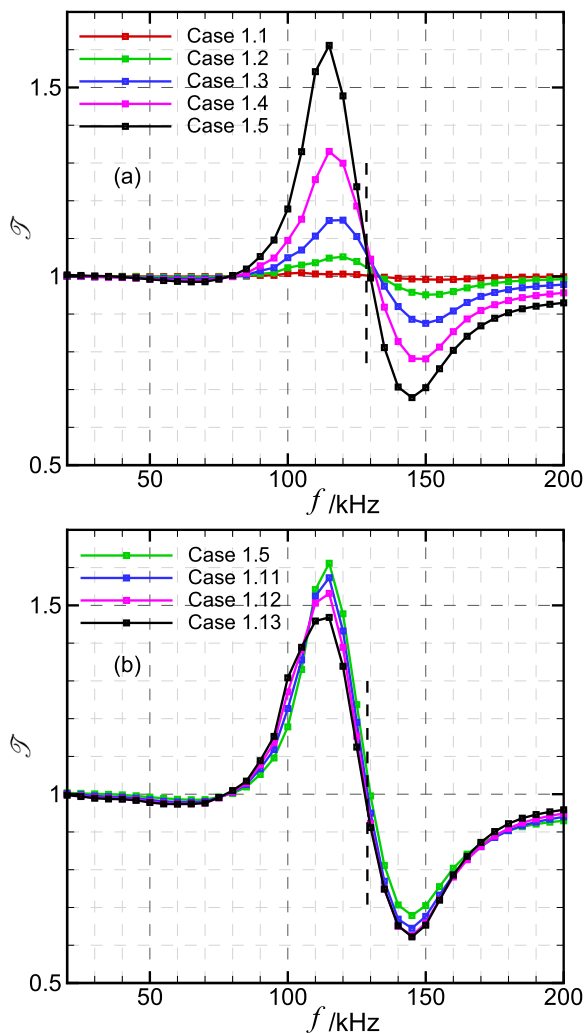


FIG. 11. Dependence of the transmission coefficient on the frequency of the oncoming mode for different hump heights h/δ_{99} (a) and widths d/δ_{99} (b). The vertical dashed line denotes the synchronization frequency.

as shown in Fig. 9. A slight discrepancy appears at $x^* = 175$ mm, indicating a relatively weak scattering effect induced by the hump. At the hump center $x^* = 185$ mm, the deviation from the smooth case is more remarkable and behaves differently for the two frequencies, i.e., for a sub-synchronization frequency, the perturbation in the near wall region is enhanced by the hump in comparison with the smooth case, but for a super-synchronization frequency, the near-wall perturbation is suppressed. Such trend provides a detailed explanation for the kinks of the red solid lines in Fig. 9, i.e., if the perturbation is enhanced locally, the amplitude will undergo a sharp increase in the close neighbourhood of the roughness, leading to a destabilizing effect as observed in Figs. 9(a) and 9(b), while a suppression of the perturbation locally for the super-synchronization frequency consequently leads to a stabilizing effect as shown in Fig. 9(d). At a sufficiently downstream location $x^* = 300$ mm, the perturbation profiles tend to recover to the unscattered state, but the amplitude undergoes a shift by a factor \mathcal{T} .

By changing the frequency f of the oncoming instability modes and repeating the above calculations, we are able to obtain the dependence of \mathcal{T} on f for different roughness sizes, as shown in Fig. 11. In general, the frequency space is divided into three zones. (i) For frequency lower than a certain value, say 80 kHz for case 1.5, which corresponds to a relatively long-wavelength first mode, \mathcal{T} is approximately 1, for which the scattering effect of the roughness is rather weak. (ii) The second zone for the current configuration is $80 \text{ kHz} < f < f_s$, in which the role played by the roughness is destabilizing ($\mathcal{T} > 1$). The transmission coefficient \mathcal{T} peaks at about 115 kHz, which corresponds to the local maximum of the phase speed of mode S, as shown in Fig. 6(a). (iii) In the region above the synchronization frequency f_s , the transmission coefficient is less than 1, indicating a stabilizing role. \mathcal{T} valleys at about $f = 145$ kHz, which corresponds to the local minimum of the phase speed of mode S. In the latter two zones, the scattering effect is more significant for a higher hump,

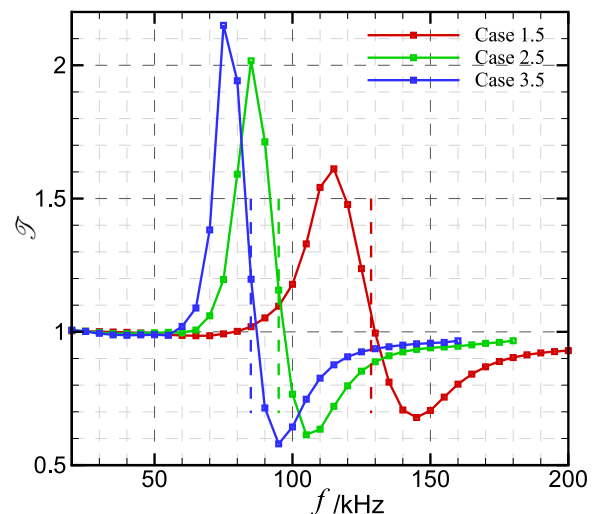


FIG. 12. Dependence of the transmission coefficient on the frequency of perturbation and the location of roughness with $d/\delta_{99} = 2$ and $h/\delta_{99} = 0.25$. The vertical dashed lines denote the corresponding synchronization frequencies at the locations.

but the width of the hump does not affect \mathcal{T} much. Such observation qualitatively agrees with the Refs. 31–34, although quantitative transmission coefficients are not introduced in those studies.

For the same size of the roughness ($h/\delta_{99} = 0.25$ and $d/\delta_{99} = 2$), Fig. 12 displays the dependence of the transmission coefficient on the Reynolds number, or L ; see the parameters in Table III. As expected, the three typical frequency zones are observed at each Re . As the roughness moves downstream (Re increases), the synchronization frequency decreases, and so the curve of $\mathcal{T}(f)$ is shifted to the decreasing-frequency direction. It is also found that the intensity of the most remarkable scattering effect $|\mathcal{T} - 1|$ increases with Re . Such observation may be related to the increase of the boundary-layer thickness δ_{99} , as well as the height of the roughness h , with Re (because we have fixed h/δ_{99} as a constant).

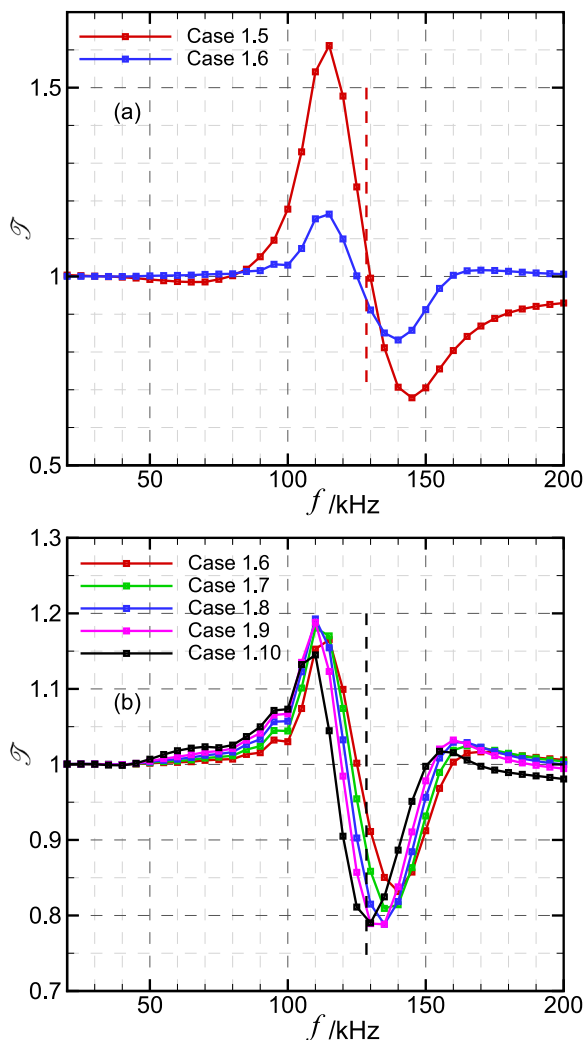


FIG. 13. Dependence of the transmission coefficient on the frequency of perturbation and the height/depth h/δ_{99} of roughness. Panel (a) is for cases 1.5–1.6 and (b) for cases 1.6–1.10. The vertical dashed line denotes the synchronization frequency.

Figure 13(a) compares the impact of a hump and an indentation with the same shape ($h/\delta_{99} = \pm 0.25$ and $d/\delta_{99} = 2$; see cases 1.5 and 1.6 in Table III) on the instability modes for $Re = 2.442 \times 10^6$. The three frequency regions, i.e., $\mathcal{T} \approx 1$, $\mathcal{T} > 1$, and $\mathcal{T} < 1$, are observed for both cases, but the scattering effect is much weaker for an indentation for most of the frequencies. The exceptional frequency band is restricted in the vicinity of the crossover frequency of the second and third zones because a slight difference of the crossover frequency appears between the hump and indentation cases. This agrees with the scattering study of the T-S wave in subsonic boundary layers by Ref. 23, i.e., an indentation does not cause an inverse scattering effect of a hump, but the scattering effect is much weaker. However, the difference is that the destabilizing effect emerges for all frequencies in the subsonic regime but appears only in a selected frequency range in the hypersonic regime. Figure 13(b)

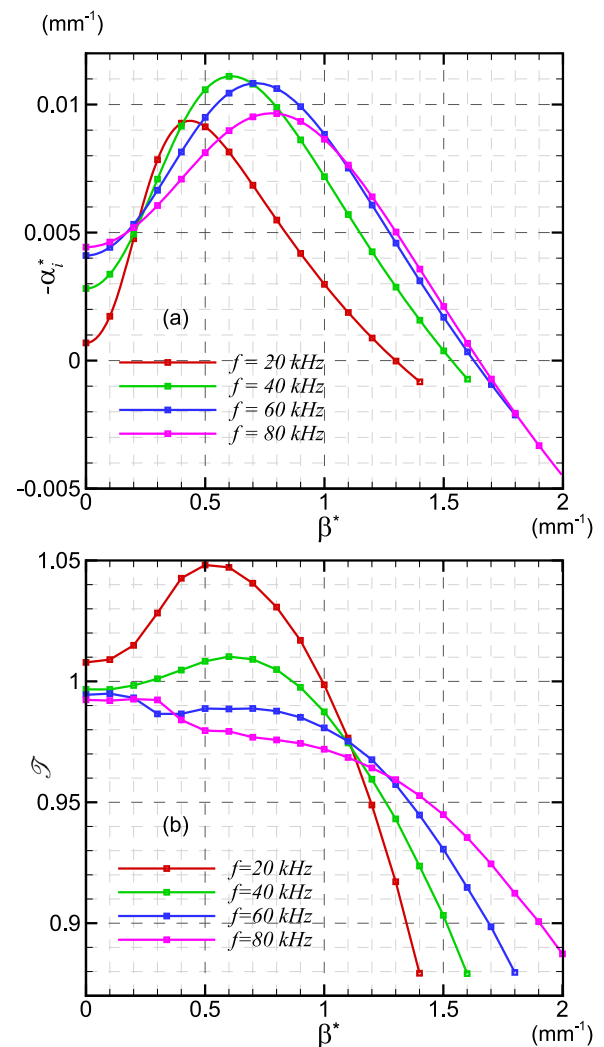


FIG. 14. Dependence of the streamwise growth rate $-\alpha_i^*$ at the location $x^* = 185$ mm (a) and the transmission coefficients (b) on the spanwise wavenumber β^* for specified frequencies of $f = 20, 40, 60$, and 80 kHz.

compares the effects of the depth of different indentations on the hypersonic modes for $Re = 2.442 \times 10^6$, and the parameters are from cases 1.6-1.10 of Table III. The crossover frequency that separates the scattering effect from destabilizing to stabilizing becomes lower as the indentation depth increases, but the scattering effect does not undergo an apparent increase.

Since the first mode usually reaches the maximum growth rate at a three-dimensional case [see Fig. 14(a)], we also study the dependence of the transmission coefficient on the spanwise wavenumber β , as shown in Fig. 14(b). The roughness parameters are $h/\delta_{99} = 0.25$, $d/\delta_{99} = 2$, and $L = 185$ mm. The wave angles $[\Theta \equiv \arctan(\beta/\alpha_r)]$ of these 3-D waves which are calculated at the location $x^* = 185$ mm fall in the range of 0–1.45, which is much smaller than $\sqrt{Ma^2 - 1}$. The implication is that the instability modes considered here belong to the inviscid regime according to Smith.³⁰ For a moderate f , \mathcal{T} decreases with β monotonically, implying a stronger suppression effect. However, for a very low frequency, the instability mode could be enhanced at a certain region of β .

IV. SUMMARY AND CONCLUSIONS

It has been long accepted that, as a typical wall imperfection, roughness may promote boundary-layer transition in the subsonic/incompressible regime due to its destabilization effect on viscous Tollmien-Schlichting modes.^{23,50} However, in the hypersonic regime, the inviscid Mack modes may be suppressed by surface roughness in a certain frequency range.^{31,33,34} In order to demonstrate the scattering mechanism and provide a parametric study on the impact of a roughness element on hypersonic boundary-layer instability, this paper develops a numerical approach based on HLNS equations. As the oncoming boundary-layer modes propagate through an inhomogeneous mean flow that is distorted by the roughness, the ensuring scattering induces a rapid distortion of the perturbation field in the close neighbourhood of the roughness and enhances or suppresses its amplitude in the downstream limit, leading to a promotion or delay of laminar-turbulent transition. This is an elliptic problem when the width of the roughness is comparable with the oncoming-perturbation wavelength. Therefore, linear stability theory (LST) and LPSE approaches do not apply, especially when a moderate separation zone appears, and only the HLNS approach is capable of accommodating the ellipticity of the scattering system. This argument is proved in this paper by comparing the numerical results with DNS results (see Fig. 8). On the other hand, the superiority of HLNS to DNS is that the former only needs a tiny computational cost for solving the high-dimensional linear-equation system without losing any accuracy as long as the amplitude of the perturbation is sufficiently small.

A transmission coefficient \mathcal{T} , as developed by Wu and Dong,²³ is introduced to characterize the role played by the roughness in the oncoming hypersonic boundary-layer modes. The oncoming Mach number is selected as 5.92 in the case studies, and the dependence of the transmission coefficient on the frequency and the oblique angle of the oncoming mode and the size and location of the hump/indentation is exhibited systematically. Being different from the traditional DNS studies,^{33,34} the whole picture of the scattering mechanism in the hypersonic regime is drawn. The frequency space is divided into three sub-regions according to the scattering

role played by the roughness. The first range corresponds to the long-wavelength first mode, which exhibits a rather weak scattering effect, i.e., $\mathcal{T} \approx 1$; in the second range, a moderate destabilizing effect of the roughness is observed, i.e., $\mathcal{T} > 1$; the roughness plays a stabilizing role in the third range, i.e., $\mathcal{T} < 1$. The interface between the latter two is located at (or close to) the synchronization frequency, which agrees with that of Fong *et al.*^{33,34} An increase of the hump height leads to an enhancement of the scattering effect, while the width of the hump does not vary the transmission coefficient much. An indentation produces less scattering effects than a hump with the same roughness size. By fixing the normalized size of the humps (d/δ_{99} and h/δ_{99}), it is found that an increase of the Reynolds number leads to the enhancement of the scattering effect. Since the 3-D first mode may be more unstable, we also consider the impact of the spanwise wavenumber β on the scattering effect. For most of the frequencies of the first mode, the stabilizing effect increases with β , except when the frequency is extremely low.

It needs to be mentioned that the HLNS approach employed in this paper is also adequate to investigate the scattering effect induced by other abrupt changes on the wall, such as a step, a suction/injection slot, a corner, and a compliant wall, which may provide valuable support for the laminar-flow control in the design of high-speed aircraft.

ACKNOWLEDGMENTS

This research was supported by NSFC (Grant No. 11772224), CARD Fundamental and Frontier Technology Research Fund (Grant No. PJD20170196), and CARD FengLei Youth Innovation Fund (Grant No. PJD20170190).

APPENDIX A: COEFFICIENT MATRICES OF (5)

The non-zero members of Γ , C , and D are

$$\Gamma_{11} = 1, \quad \Gamma_{22} = \bar{\rho}, \quad \Gamma_{33} = \bar{\rho}, \quad \Gamma_{44} = \bar{\rho},$$

$$\Gamma_{51} = \bar{T}(1 - \gamma)/\gamma, \quad \Gamma_{55} = \bar{\rho}/\gamma,$$

$$c_{14} = \bar{\rho}, \quad c_{24} = 2\bar{\mu}_x/(3Re), \quad c_{34} = 2\bar{\mu}_y/(3Re),$$

$$c_{41} = \bar{T}/(\gamma Ma^2), \quad c_{42} = -\bar{\mu}_x/Re, \quad c_{43} = -\bar{\mu}_y/Re,$$

$$c_{45} = \bar{\rho}/(\gamma Ma^2) - \bar{\mu}_T \bar{s}_{33}/Re,$$

$$c_{54} = 2(1 - \gamma)\bar{\mu} Ma^2 \bar{s}_{33}/Re,$$

$$d_{11} = \bar{u}_x + \bar{v}_y, \quad d_{12} = \bar{\rho}_x, \quad d_{13} = \bar{\rho}_y,$$

$$d_{21} = \bar{u}\bar{u}_x + \bar{v}\bar{u}_y + \bar{T}_x/(\gamma Ma^2), \quad d_{22} = \bar{\rho}\bar{u}_x,$$

$$d_{23} = \bar{\rho}\bar{u}_y, \quad d_{31} = \bar{u}\bar{v}_x + \bar{v}\bar{v}_y + \bar{T}_y/(\gamma Ma^2),$$

$$d_{32} = \bar{\rho}\bar{v}_x, \quad d_{33} = \bar{\rho}\bar{v}_y, \quad d_{51} = (\bar{u}\bar{T}_x + \bar{v}\bar{T}_y)/\gamma,$$

$$d_{52} = \bar{\rho}\bar{T}_x/\gamma + \bar{T}\bar{\rho}_x(1 - \gamma)/\gamma,$$

$$d_{53} = \bar{\rho}\bar{T}_y/\gamma + \bar{T}\bar{\rho}_y(1 - \gamma)/\gamma,$$

$$\begin{aligned}
 d_{25} &= \bar{\rho}_x / (\gamma Ma^2) - \bar{\mu}_T [\nabla^2 \bar{u} + \frac{1}{3} (\frac{\partial^2 \bar{u}}{\partial x^2} + \frac{\partial^2 \bar{v}}{\partial x \partial y})] / Re \\
 &\quad - [\bar{s}_{11} \frac{\partial \bar{\mu}_T}{\partial x} + \bar{s}_{12} \frac{\partial \bar{\mu}_T}{\partial y}] / Re, \\
 d_{35} &= \bar{\rho}_y / (\gamma Ma^2) - \bar{\mu}_T [\nabla^2 \bar{v} + \frac{1}{3} (\frac{\partial^2 \bar{v}}{\partial y^2} + \frac{\partial^2 \bar{u}}{\partial x \partial y})] / Re \\
 &\quad - [\bar{s}_{12} \frac{\partial \bar{\mu}_T}{\partial x} + \bar{s}_{22} \frac{\partial \bar{\mu}_T}{\partial y}] / Re, \\
 d_{55} &= (\bar{u} \bar{\rho}_x + \bar{v} \bar{\rho}_y) (1 - \gamma) / \gamma - (\bar{\mu}_T \nabla^2 \bar{T} + \nabla \bar{T} \cdot \nabla \bar{\mu}_T) / (Re Pr) \\
 &\quad + (1 - \gamma) Ma^2 \bar{\mu}_T [2(\bar{u}_x - \bar{v}_y)^2 + 2\bar{u}_x^2 + 2\bar{v}_y^2 + 3\bar{s}_{12}^2] / (3Re),
 \end{aligned}$$

where

$$\begin{aligned}
 \bar{s}_{11} &= (4\bar{u}_x - 2\bar{v}_y) / 3, \quad \bar{s}_{22} = (4\bar{v}_y - 2\bar{u}_x) / 3, \\
 \bar{s}_{33} &= -2/3(\bar{u}_x + \bar{v}_y), \quad \bar{s}_{12} = \bar{u}_y + \bar{v}_x, \quad \bar{\mu}_T = d\bar{\mu}/dT.
 \end{aligned}$$

The other matrices are

$$\begin{aligned}
 \bar{\mathbf{A}} &= \xi_x \mathbf{A} + \xi_y \mathbf{B} + (\xi_x \xi_{x,\xi} + \eta_x \xi_{x,\eta}) \mathbf{V}_{xx} \\
 &\quad + (\xi_y \xi_{y,\xi} + \eta_y \xi_{y,\eta}) \mathbf{V}_{yy} + (\xi_x \xi_{y,\xi} + \eta_x \xi_{y,\eta}) \mathbf{V}_{xy}, \\
 \bar{\mathbf{B}} &= \eta_x \mathbf{A} + \eta_y \mathbf{B} + (\xi_x \eta_{x,\xi} + \eta_x \eta_{x,\eta}) \mathbf{V}_{xx} \\
 &\quad + (\xi_y \eta_{y,\xi} + \eta_y \eta_{y,\eta}) \mathbf{V}_{yy} + (\xi_x \eta_{y,\xi} + \eta_x \eta_{y,\eta}) \mathbf{V}_{xy}, \\
 \mathbf{V}_{\xi\xi} &= \xi_x^2 \mathbf{V}_{xx} + \xi_y^2 \mathbf{V}_{yy} + \xi_x \xi_y \mathbf{V}_{xy}, \\
 \mathbf{V}_{\eta\eta} &= \eta_x^2 \mathbf{V}_{xx} + \eta_y^2 \mathbf{V}_{yy} + \eta_x \eta_y \mathbf{V}_{xy}, \\
 \mathbf{V}_{\xi\eta} &= 2\xi_x \eta_x \mathbf{V}_{xx} + 2\xi_y \eta_y \mathbf{V}_{yy} + (\xi_x \eta_y + \xi_y \eta_x) \mathbf{V}_{xy}, \\
 \mathbf{V}_{\xi z} &= \xi_x \mathbf{V}_{xz} + \xi_y \mathbf{V}_{yz}, \quad \mathbf{V}_{\eta z} = \eta_x \mathbf{V}_{xz} + \eta_y \mathbf{V}_{yz}, \\
 \mathbf{V}_{zz} &= -(\bar{\mu}/Re) \text{diag}(0, 1, 1, 4/3, 1/Pr),
 \end{aligned}$$

where

$$\begin{aligned}
 \mathbf{V}_{xx} &= -(\bar{\mu}/Re) \text{diag}(0, 4/3, 1, 1, 1/Pr), \\
 \mathbf{V}_{yy} &= -(\bar{\mu}/Re) \text{diag}(0, 1, 4/3, 1, 1/Pr),
 \end{aligned}$$

the non-zero members of \mathbf{V}_{xy} , \mathbf{V}_{xz} , and \mathbf{V}_{yz} are $V_{xy,23} = V_{xy,32} = V_{xz,24} = V_{xz,42} = V_{yz,34} = V_{yz,43} = -\bar{\mu}/(3Re)$.

The non-zero members of \mathbf{A} and \mathbf{B} are

$$\begin{aligned}
 a_{11} &= \bar{u}, \quad a_{12} = \bar{p}, \quad a_{21} = \bar{T}/(\gamma Ma^2), \\
 a_{22} &= \bar{\rho} \bar{u} - 4\bar{\mu}_x / (3Re), \quad a_{23} = -\bar{\mu}_y / Re, \\
 a_{25} &= \bar{\rho} / (\gamma Ma^2) - (\bar{\mu}_T / Re) \bar{s}_{11}, \quad a_{32} = 2\bar{\mu}_y / (3Re), \\
 a_{33} &= \bar{\rho} \bar{u} - \bar{\mu}_x / Re, \quad a_{35} = -(\bar{\mu}_T / Re) \bar{s}_{12}, \\
 a_{44} &= \bar{\rho} \bar{u} - \bar{\mu}_x / Re, \quad a_{51} = \bar{u} \bar{T} (1 - \gamma) / \gamma, \\
 a_{52} &= 2(1 - \gamma) \bar{\mu} Ma^2 \bar{s}_{11} / Re, \\
 a_{53} &= 2(1 - \gamma) \bar{\mu} Ma^2 \bar{s}_{12} / Re, \\
 a_{55} &= \bar{\rho} \bar{u} / \gamma - 2\bar{\mu}_x / (Re Pr),
 \end{aligned}$$

$$\begin{aligned}
 b_{11} &= \bar{v}, \quad b_{13} = \bar{p}, \quad b_{22} = \bar{\rho} \bar{v} - \bar{\mu}_y / Re, \\
 b_{23} &= 2\bar{\mu}_x / (3Re), \quad b_{25} = -\bar{\mu}_T \bar{s}_{12} / Re, \\
 b_{31} &= \bar{T} / (\gamma Ma^2), \quad b_{32} = -\bar{\mu}_x / Re, \\
 b_{33} &= \bar{\rho} \bar{v} - 4\bar{\mu}_y / (3Re), \quad b_{35} = \bar{\rho} / (\gamma Ma^2) - \bar{\mu}_T / \bar{s}_{22} Re, \\
 b_{44} &= \bar{\rho} \bar{v} - \bar{\mu}_y / Re, \quad b_{51} = \bar{v} \bar{T} (1 - \gamma) / \gamma, \\
 b_{52} &= 2(1 - \gamma) \bar{\mu} Ma^2 \bar{s}_{12} / Re, \\
 b_{53} &= 2(1 - \gamma) \bar{\mu} Ma^2 \bar{s}_{22} / Re, \\
 b_{55} &= \bar{\rho} \bar{v} / \gamma - 2\bar{\mu}_y / (Re Pr).
 \end{aligned}$$

APPENDIX B: DISCRETIZATION SCHEMES USED FOR (7)

The partial derivative of $\tilde{\phi}(\xi, \eta)$ with respect to ξ is discretized as

$$\frac{\partial \tilde{\phi}_{ij}}{\partial \xi} = \sum_{l=s}^{s+p} a_{il} \tilde{\phi}_{lj}, \quad \frac{\partial^2 \tilde{\phi}_{ij}}{\partial \xi^2} = \sum_{l=s}^{s+p} b_{il} \tilde{\phi}_{lj},$$

with

$$s = \begin{cases} 0, & i \in [0, 2], \\ i - p/2, & i \in [3, I - 3], \\ I - p, & i \in [I - 2, I], \end{cases}$$

where p (set to 4) is the order of the scheme determining the stencil of the difference scheme, and a_{il} , b_{il} are the coefficients determined by the Lagrange interpolation, i.e.,

$$a_{il} = \sum_{m=s, m \neq i}^{s+p} \frac{1}{\xi_i - \xi_m} \prod_{k=s, k \neq i}^{s+p} \frac{\xi_i - \xi_k}{\xi_l - \xi_k}, \quad (B1)$$

$$b_{il} = \sum_{n=s}^{s+p} \sum_{m=s}^{s+p} \frac{1}{(\xi_i - \xi_m)(\xi_i - \xi_n)} \prod_{k=s, k \neq i}^{s+p} \frac{\xi_i - \xi_k}{\xi_l - \xi_k} \quad (B2)$$

for $m \neq i$, $n \neq i$, and $m \neq n$.

The partial derivative of $\tilde{\phi}(\xi, \eta)$ with respect to η follows the same form, and the mixed partial derivative is discretized as

$$\frac{\partial^2 \tilde{\phi}_{ij}}{\partial \xi \partial \eta} = \sum_{l=s}^{s+p} \sum_{m=s}^{s+p} a_{ilm} \tilde{\phi}_{lm}.$$

APPENDIX C: RESOLUTION STUDY FOR HLNS APPROACH

In order to confirm the mesh system adopted in this paper to be sufficient, we choose cases 1.5 (the highest hump in the current paper) and 1.10 (the deepest indentation) with three typical frequencies ($f = 70, 110$, and 140 kHz), and perform HLNS calculations by reducing the width of the grid points in the streamwise direction to $dx = 0.5\Delta x$ and increasing the number of grid points in the wall-normal direction to $J = 500$, as shown in Fig. 15. It is found that the calculated amplitude evolution of the temperature fluctuations overlaps with that of the original mesh system ($J = 300$ and $dx = \Delta x$) precisely, indicating the reliability of the calculations in the current paper.

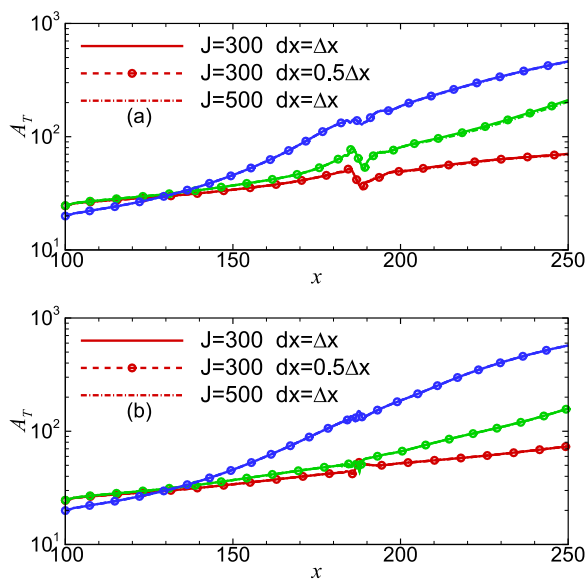


FIG. 15. Amplitude-evolution of the temperature fluctuations for case 1.5 (a) and case 1.10 (b) at frequencies of $f = 70$ kHz (red), 110 kHz (green), and 140 kHz (blue), where the solid lines are for the standard mesh, the symbolized dashed lines are for the mesh refined in the x direction and the dashed-dotted lines are for the mesh refined in the y direction.

REFERENCES

- ¹E. Van Driest and W. McCauley, "Measurements of the effect of two-dimensional and three-dimensional roughness elements on boundary layer transition," *J. Aerosp. Sci.* **27**, 261–271 (1960).
- ²S. P. Schneider, "Effects of roughness on hypersonic boundary-layer transition," *J. Spacecr. Rockets* **45**, 193–209 (2008).
- ³P. V. Chuvakhov, "Controlled experiment on isolated roughness-induced transition in sharp flat plate hypersonic flows," *AIP Conf. Proc.* **2027**, 030160 (2018).
- ⁴B. Wheaton and S. Schneider, "Roughness-induced instability in a laminar boundary layer at Mach 6," AIAA Paper 2010-1574, 2010.
- ⁵S. P. Schneider, "Developing mechanism-based methods for estimating hypersonic boundary-layer transition in flight: The role of quiet tunnels," AIAA Paper 2013-2608, 2013.
- ⁶Y. Gromyko, D. Bountin, P. Polivanov, A. Sidorenko, and A. Maslov, "The effect of roughness of blunted nose of cone on the development of disturbances and laminar-turbulent transition in a hypersonic boundary layer," *AIP Conf. Proc.* **1893**, 030148 (2017).
- ⁷D. Bountin, Y. V. Gromyko, P. Polivanov, and A. Maslov, "Influence of roughness of cone nose-tip on laminar-turbulent transition at hypersonic speed," *AIP Conf. Proc.* **2027**, 030005 (2018).
- ⁸N. A. Denissen and E. B. White, "Secondary instability of roughness-induced transient growth," *Phys. Fluids* **25**, 114108 (2013).
- ⁹N. De Tullio, P. Paredes, N. Sandham, and V. Theofilis, "Laminar-turbulent transition induced by a discrete roughness element in a supersonic boundary layer," *J. Fluid Mech.* **735**, 613–646 (2013).
- ¹⁰N. De Tullio and N. D. Sandham, "Influence of boundary-layer disturbances on the instability of a roughness wake in a high-speed boundary layer," *J. Fluid Mech.* **763**, 136–165 (2015).
- ¹¹P. Drazin and W. Reid, *Hydrodynamic Instabilities* (Cambridge University Press, Cambridge, 1981).
- ¹²L. M. Mack, "Review of linear compressible stability theory," in *Stability of Time Dependent and Spatially Varying Flows* (Springer, 1987), pp. 164–187.
- ¹³A. H. Nayfeh, S. A. Ragab, and A. A. Al-Maaitah, "Effect of bulges on the stability of boundary layers," *Phys. Fluids* **31**, 796–806 (1988).
- ¹⁴T. Cebeci and D. A. Egan, "Prediction of transition due to isolated roughness," *AIAA J.* **27**, 870–875 (1989).
- ¹⁵A. A. Al-Maaitah, A. H. Nayfeh, and S. A. Ragab, "Effect of wall cooling on the stability of compressible subsonic flows over smooth humps and backward-facing steps," *Phys. Fluids A* **2**, 381–389 (1990).
- ¹⁶J. A. Masad and V. Iyer, "Transition prediction and control in subsonic flow over a hump," *Phys. Fluids* **6**, 313–327 (1994).
- ¹⁷D. Park and S. O. Park, "Linear and non-linear stability analysis of incompressible boundary layer over a two-dimensional hump," *Comput. Fluids* **73**, 80–96 (2013).
- ¹⁸P. Holloway and J. Sterrett, "Effect of controlled surface roughness on boundary-layer transition and heat transfer at Mach number of 4.8 and 6.0," Technical Report D-2054, NASA Technical Note, 1964.
- ¹⁹K. Fujii, "Experiment of the two-dimensional roughness effect on hypersonic boundary-layer transition," *J. Spacecr. Rockets* **43**, 731–738 (2006).
- ²⁰A. Fedorov, "Receptivity of hypersonic boundary layer to acoustic disturbances scattered by surface roughness," AIAA Paper 2003-3731, 2003.
- ²¹A. V. Fedorov, "Receptivity of a high-speed boundary layer to acoustic disturbances," *J. Fluid Mech.* **491**, 101–129 (2003).
- ²²M. Goldstein and P. Ricco, "Non-localized boundary layer instabilities resulting from leading edge receptivity at moderate supersonic Mach numbers," *J. Fluid Mech.* **838**, 435–477 (2018).
- ²³X. Wu and M. Dong, "A local scattering theory for the effects of isolated roughness on boundary-layer instability and transition: Transmission coefficient as an eigenvalue," *J. Fluid Mech.* **794**, 68–108 (2016).
- ²⁴M. Dong and X. Wu, "Local scattering theory and the role of an abrupt change on boundary-layer instability and acoustic radiation," AIAA Paper 2016-3194, 2016.
- ²⁵M. Dong and X. Wu, "Generation of convective instability modes in the near-wake flow of the trailing edge of a flat plate," AIAA Paper 2017-4022, 2017.
- ²⁶M. Dong and A. Zhang, "Scattering of Tollmien-Schlichting waves as they pass over forward-/backward-facing steps," *Appl. Math. Mech.* **39**, 1411–1424 (2018).
- ²⁷J. Perraud, D. Arnal, A. Seraudie, and D. Tran, "Laminar-turbulent transition on aerodynamic surfaces with imperfections," in RTO-AVT-111 Symposium, 2004.
- ²⁸Y. Wang and M. Gaster, "Effect of surface steps on boundary layer transition," *Exp. Fluids* **39**, 679–686 (2005).
- ²⁹J. Perraud, D. Arnal, and W. Kuehn, "Laminar-turbulent transition prediction in the presence of surface imperfections," *Int. J. Eng. Syst. Modell. Simul.* **6**, 162–170 (2014).
- ³⁰F. Smith, "On the first-mode instability in subsonic, supersonic or hypersonic boundary layers," *J. Fluid Mech.* **198**, 127–153 (1989).
- ³¹O. Marxen, G. Iaccarino, and E. S. Shaqfeh, "Disturbance evolution in a Mach 4.8 boundary layer with two-dimensional roughness-induced separation and shock," *J. Fluid Mech.* **648**, 435–469 (2010).
- ³²L. Duan, X. Wang, and X. Zhong, "Stabilization of a Mach 5.92 boundary layer by two-dimensional finite-height roughness," *AIAA J.* **51**, 266–270 (2013).
- ³³K. D. Fong, X. Wang, and X. Zhong, "Numerical simulation of roughness effect on the stability of a hypersonic boundary layer," *Comput. Fluids* **96**, 350–367 (2014).
- ³⁴K. D. Fong, X. Wang, and X. Zhong, "Parametric study on stabilization of hypersonic boundary layer waves using 2-D surface roughness," AIAA Paper 2015-0837, 2015.
- ³⁵A. Fedorov, "Transition and stability of high-speed boundary layers," *Annu. Rev. Fluid Mech.* **43**, 79–95 (2011).
- ³⁶J. Sawaya, V. Sannas, S. Yassir, A. Sescu, and M. Visbal, "Assessment of the impact of two-dimensional wall deformation shape on high-speed boundary-layer disturbances," *AIAA J.* **56**, 4787–4800 (2018).
- ³⁷K. D. Fong, X. Wang, Y. Huang, X. Zhong, G. R. McKiernan, R. A. Fisher, and S. P. Schneider, "Second mode suppression in hypersonic boundary layer by roughness: Design and experiments," *AIAA J.* **53**, 3138–3144 (2015).

- ³⁸Q. Tang, Y. Zhu, X. Chen, and C. Lee, "Development of second-mode instability in a Mach 6 flat plate boundary layer with two-dimensional roughness," *Phys. Fluids* **27**, 064105 (2015).
- ³⁹D. Park and S. O. Park, "Study of effect of a smooth hump on hypersonic boundary layer instability," *Theor. Comput. Fluid Dyn.* **30**, 543–563 (2016).
- ⁴⁰K. D. Fong and X. Zhong, "DNS and PSE study on the stabilization effect of hypersonic boundary layer waves using 2-D surface roughness," AIAA Paper 2016-3347, 2016.
- ⁴¹H. Raposo, S. Mughal, and R. Ashworth, "Acoustic receptivity and transition modeling of Tollmien-Schlichting disturbances induced by distributed surface roughness," *Phys. Fluids* **30**, 044105 (2018).
- ⁴²Z. Huang and X. Wu, "A local scattering approach for the effects of abrupt changes on boundary-layer instability and transition: A finite-Reynolds-number formulation for isolated distortions," *J. Fluid Mech.* **822**, 444–483 (2017).
- ⁴³D. Park and S. O. Park, "Influence of two-dimensional smooth humps on linear and non-linear instability of a supersonic boundary layer," *Comput. Fluids* **79**, 140–149 (2013).
- ⁴⁴L. Zhao, C. Zhang, J. Liu, and J. Luo, "Improved algorithm for solving nonlinear parabolized stability equations," *Chin. Phys. B* **25**, 084701 (2016).
- ⁴⁵L. Zhao, "Study on instability of stationary crossflow vortices in hypersonic swept blunt plate boundary layer," Ph.D. thesis, Tianjin University, 2017 (in Chinese).
- ⁴⁶X. Wu and M. Dong, "Entrainment of short-wavelength free-stream vortical disturbances in compressible and incompressible boundary layers," *J. Fluid Mech.* **797**, 683–728 (2016).
- ⁴⁷M. R. Malik, "Finite-difference solution of the compressible stability eigenvalue problem," NASA Technical Report 16572, 1982.
- ⁴⁸A. Fedorov and A. Tumin, "Initial-value problem for hypersonic boundary-layer flows," *AIAA J.* **41**, 379–389 (2003).
- ⁴⁹C.-L. Chang and M. R. Malik, "Linear and nonlinear PSE for compressible boundary layers," Technical Report 191537, NASA Contractor Report, 1993.
- ⁵⁰H. Xu, S. J. Sherwin, P. Hall, and X. Wu, "The behaviour of Tollmien-Schlichting waves undergoing small-scale localised distortions," *J. Fluid Mech.* **792**, 499–525 (2016).